*Manuscript
Click here to view linked References

Hierarchical Composites of B_4C-TiB_2 eutectic particles reinforced with Ti

I. Solodkyi[(a, b*)], I. Bogomol[(a)], V. Bolbut[(c)], P. Loboda[(a)], A. Kuncser[(d)], O. Vasylkiv[(b, *)], P. Badica[(d, *)]

[(a)]National Technical University of Ukraine "Igor Sikorsky Kyiv Polytechnic Institute", Peremogy Ave. 37, 03056Kyiv, Ukraine

[(b)]National Institute for Materials Science, 1–2–1 Sengen, Tsukuba, Ibaraki 305–0047, Japan

[(c)]Otto von Guericke University Magdeburg, Universitätsplatz 2, 39106 Magdeburg, Germany

[(d)]National Institute of Materials Physics, Atomistilor 405 A, 077125 Magurele, Romania

Corresponding Authors:

Ievgen Solodkyi, solodkyi@iff.kpi.ua, phone +38-(0)66-1191899

Oleg Vasylkiv, oleg.vasylkiv@nims.go.jp /phone +81-(0)80-41444747

Petre Badica, badica2003@yahoo.com /phone: +40-(0)21-3690185

Submitted to Ceramics International, Elsevier.

Abstract

Eutectic particles of B_4C-TiB_2 were reinforced with Ti by spark plasma sintering (SPS) or infiltration. The SPSed samples with 20, 30 and 40 wt. % Ti consisted of ceramic phase, and had a bicontinuous macrostructure formed by the Ti-rich region and the eutectic particles region, while the infiltrated sample was a complex composite comprised of a 3D Ti-rich continuous network, composite in nature, that contained Ti-metal and in which are embedded isolated ceramic (eutectic) particles. The SPSed samples are brittle with the maximum bending strength of 300 MPa for the 30 wt. % Ti, higher than for a reference sample produced by SPS from directionally solidified eutectic particles. A higher amount of added Ti results in a higher displacement in the bending test suggesting a higher fracture toughness. Simultaneous strengthening and toughening of the composite was realized. The infiltrated sample was ductile, while its bending strength (220 MPa) was comparable to the values measured for the brittle as-introduced reference sample and the sample with 20 wt. % Ti, both produced by SPS. In the SPSed and infiltrated samples at the interface between the Ti-rich region and B_4C-TiB_2 eutectic particles, a local 'pull-out' intergranular fracturing mechanism mainly involving Ti-B 1D-grains was observed. This local micromechanism together with a 'pull out' macromechanism of the eutectic grains from the Ti-rich component are considered important for the bridging/anchoring behavior responsible for the strengthening and toughening processes in our novel hierarchical composites.

Keywords: B_4C-TiB_2 eutectic, Ti reinforcement, bending test, hierarchical composites, spark plasma sintering, infiltration

1. Introduction

The microstructure of composites viewed at different levels allows property control and optimization for a specific application. In many cases, there are at least two functional parameters with opposite tendencies that should be simultaneously improved for a superior general performance. The straightforward example is the need for composites with a high ductility or fracture toughness and strength or strength-to-weight ratio [1]. To achieve this goal, the literature presents different solutions in which the microstructural concept is defined as a range of uniquely multi-scale hierarchical structures obtained as a result of planning, design, and use of adequate processing technologies [see, e.g., review article 2 and refs. therein]. Under these circumstances, selection of the building elements of a composite, their compatibility, relationships, arrangement and how these elements and their structures are formed considering the raw materials, are essential.

In the two-phase typical *m*etal *m*atrix *c*omposites (MMC), the strategy is to take advantage of the soft-metal matrix and hard-ceramic reinforcement phases leading to improvements in the mechanical properties that are not achievable for the individual phases. The soft metal provides the plastic regions in the composite ensuring a high toughness and ductility, while the hard reinforcement elements contribute to strengthening. The classic image is that the metal forms a continuous 3D network called the matrix, while the hard elements such as boride, carbide, or intermetallic 3D particles, 1D whiskers/fibers, or 2D plates/layers are isolated and embedded in the matrix. In practice, at macro-scale level the elements of the reinforcement can also form a continuous network and confusion between the metal matrix composites and ceramic matrix composites is imminent. Different types of composite microstructures were analyzed and classified in ref. [2]. The authors proposed to define 'the phase that is the base material as the matrix phase and the phase that is added to the base material for performance/control improvement as the reinforcement'.

Considering this definition, in this study, we fabricated new composites in which the matrix is made of B_4C-TiB_2 eutectic particles and the reinforcement is Ti. The choice for using the eutectic particles in the composites is justified by the following aspects:

(i) Eutectic particles, due to their *in-situ* organized composite microstructure with TiB_2 inclusions in a B_4C crystalline environment possess a fine microstructure with a typically coherent excellent bonding between the components [3-5].

(ii) The TiB_2 inclusions show a preferential 1D shape. These details and composite nature of the eutectics promote a fracture toughness enhancement in otherwise critically brittle materials. This is also the case for the B_4C-TiB_2 eutectic; it was shown that the fracture toughness, K_{IC}, of the

directionally solidified eutectic crystals or of ceramic spark plasma sintered from such eutectic particles (5-6 MPa.m$^{1/2}$ [5-8]), is higher than for the B_4C ceramic (1-3 MPa.m$^{1/2}$ [9]), while the hardness is comparable (>30 GPa) [8-11]).

(iii) Due to the composite nature of the eutectic, the reaction between TiB_2 or B_4C from the eutectic grains with Ti reinforcement is different and it is expected to lead to a complex and mechanically favorable composite interface between the matrix and the reinforcement. The interface between the matrix and reinforcement plays an important role in defining the overall mechanical properties of the composite.

The complex microstructures of our composites are visualized by electron microscopy, and the samples are mechanically characterized by 3-point bending tests and a fractography analysis. Because in the Ti-matrix composites (e.g., reinforced with TiB whiskers) it is recognized that powder metallurgy (PM) routes do not solve the brittleness issues [2, 12], we attempted fabrication of the composites not only by powder metallurgy routes employing spark plasma sintering, but also by the infiltration technique. The powder metallurgy route allows control of the composition and of the microstructure, while by the infiltration method, compositional and microstructural control is limited. On the other hand, infiltration is more appropriate for the industrial production of the composite allowing fabrication of large parts and different shapes necessary for practical applications. At present, there is an extended interest in the Ti-B, Ti-C and Ti-B-C systems for fabrication of different composites. In general, the Ti-based materials are of paramount importance for the aerospace as well as other industries. The literature reports different examples. The TiB_2-based ceramic composites reinforced with B_4C show record high bending strengths among the covalent borides, both at room and high temperatures [13 and refs. therein]. In the B_4C-TiB_2 ceramic composites prepared from elements by milling and SPS at 1700 °C, enhancement of the fracture toughness was obtained [14]. The Ti-(Ti-B)/(Ti-C) metal-ceramic eutectic in the Ti-B-C system allowed through the Ti metal transient phase to plastically deform the sample by hot pressing into a bulk with full density before its transformation into a TiB_2-TiC ceramic composite. [15-17]. Processing was performed at temperatures as low as 1600°C. Hong et al. [18] obtained TiB_2-TiC composites by reactive sintering of the Ti metal and B_4C powders even at the lower temperature of 1500 °C. In-situ TiB whiskers and TiC particles are effective reinforcements of the Ti matrix [19-24]. However, the high volume fraction of the ceramic reinforcement required for the enhancement of the mechanical properties and limited ductility (or its loss in composites processed by powder metallurgy) work against the practical applications of Ti-TiB or Ti-TiC metal-matrix composites [12]. To overcome the problems, in refs. [25, 26] use of large and spherical Ti powders decorated with TiB_2 produced by PM a Ti-TiB composite with a TiB-network in Ti that surrounds large regions of almost pure Ti. Ductility

was preserved and a high improvement in tensile strength was achieved. The current paragraph suggests that fabrication and assessment of novel microstructures with a ceramic or metal matrix in the Ti-B-C system deserves attention. There is a limited number of articles on samples fabricated from the B_4C-TiB_2 eutectic particles. In refs. [6, 7], directionally solidified eutectic particles (B_4C-TiB_2) or powder mixtures of B_4C and $(B_4C\text{-}TiB_2)_{eutectic}$ were spark plasma sintered and have shown remarkable properties. These samples are taken as reference samples and their mechanical properties will be compared to those of the novel composites obtained in this study.

2. Experimental part

The eutectic B_4C–TiB_2 powder (grain size of 300-500 μm) was obtained by centrifugal atomization of an eutectic melt (65 wt. % B_4C and 35 wt. % TiB_2) obtained from a powder mixture of boron carbide (98 %, JSC Zaporozhabraziv, Zaporizhzhia, Ukraine) and titanium diboride (99 %, Chim Reactiv Co., Ltd., Donetsk, Ukraine). Namely, mixing of the powders was performed in a plastic jar and balls. To the mixture was added (0.15 ml/g) a water solution of polyvinyl alcohol (PVA) at a concentration of 2.5%. The additive helps bonding of the powder particles in disks of 30 mm diameter and 35 mm height, pressed at 50 MPa. The compacts were dried in a vacuum at 100°C for 3 h and sintered in a vacuum electric furnace at 1600°C for 30 min. The sintered samples were used as the raw materials (electrode, Fig. 1) in the atomization process. The details are presented elsewhere [27].

Bulk samples of $(B_4C\text{-}TiB_2)_{eutectic}$ added with Ti were obtained by two routes, infiltration and spark plasma sintering (Fig. 1).

For SPS processing (Fig. 1, follow the blue arrows), the as-processed eutectic powder was subject to grinding for 5 min with a rotation speed of 580 rpm in a planetary ball mill. Ti jars and balls were used. The weight ratio between the powder and the balls was 1:10. The grain size of the resulting eutectic powder was in the range of 50-160 μm. The eutectic powder was mixed with Ti (average particles size of 140 μm, produced by Zaporozhye Titanium & Magnesium Combine Co. Ltd., Zaporizhia, Ukraine). Powders were loaded into a plastic jar with balls. The powder to balls weight ratio was 1:5. The rotation speed was 120 rpm and the homogenization time was 30 min. The starting compositions were with 20, 30 and 40 wt. % Ti. The metal-eutectic mixture was wrapped in graphite foil (0.1 mm thickness), loaded into a graphite die with an inner diameter of 20 mm, and processed by spark plasma sintering (SPS). The die with the powder mixture was placed in an SPS furnace ‘Dr. Sinter’ SPS Syntex 1050 (Japan). An initial pressure of 5 MPa was applied to the sample to ensure a good electrical contact between the powder and the die. The pressure was increased to 50 MPa during heating to 1700 ^{o}C. This

temperature was selected to be above the melting point of Ti of 1668 deg C. The dwell time was 5 min. The heating rate was about 100 °C/min. An intermediate stabilization step with a dwell time of 1 min was undertaken at 800 °C. Cooling was to 600 °C at the rate of 100 °C/min followed by furnace cooling to room temperature.

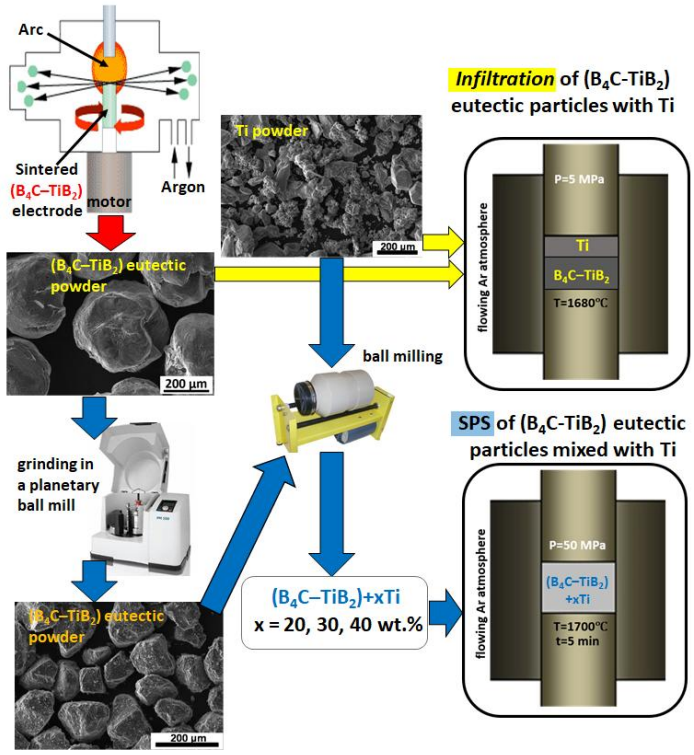

Fig. 1 Technological routes for samples preparation by infiltration (follow the yellow arrows) and spark plasma sintering (follow the blue arrows).

The sintering process was performed in a flowing Ar atmosphere at the flow rate of 2 l/min. Depending on the starting composition, the SPSed samples were denoted as SPS20, SPS30, and SPS40 (Table 1).

A sample was also prepared by infiltration. The raw eutectic B_4C-TiB_2 powder (300-500 µm) was pressed into a green body. Titanium powder was placed on top of the green body and a pressure of 5 MPa was applied (Fig. 1, follow the yellow arrows). Processing was conducted under similar atmosphere and technological parameters as for SPS samples introduced in the previous paragraph. The differences were: (i) - the maximum heating temperature was 1680 °C and (ii)– no dwell time was applied. This sample was denoted as I35 (Table 1). The bulk samples were machined by electric discharge and polished with diamond abrasives for further characterization.

Bulk density ρ of the samples was measured by Archimedes method in ethanol. The relative density was determined as $R = (\rho / \rho_t)$ x 100 % (Table 1), where ρ_t is the theoretical density. Theoretical density was calculated with the procedure from ref. [28] considering that samples have the phase composition as determined from x-ray diffraction (Table 1).

X-ray diffraction (XRD) patterns were obtained by a Rigaku Ultima IV (Japan) diffractometer (CuKα radiation λ = 1.54187 Å) over the 2θ range of 20–90°, in steps of 0.04° with a sampling time of 3 s for each step. The PDXL software was used for the Rietveld refinement.

Microstructural investigations were performed by using the scanning electron microscopes REM-106I (Selmi, Ukraine), Tescan Lyra 3, and transmission electron microscope JEM 2100 TEM.

The flexural strength was measured by a three-point bending test using a Deben Microtester (Woolpit, UK) with a span of 15 mm and the maximum load of 500 N. Experiments were carried out in air at room temperature with a load speed of 0.5 mm/min and for a pre-load of 2 N. At least 7 samples (2 mm × 2.5 mm × 20 mm) were tested per composite. The flexural strength σ_u was determined using eq. (1):

$$\sigma_u = 3Pl/2bh^2 \quad (1)$$

where P is the axial load; l - length of the support span; b – is the samples width; and h - is the sample thickness. The hardness was determined using a Vickers hardness tester (AVK-A, Akashi Co., Tokyo, Japan). Loads of 9.8 and 49 N were applied for 15 s on the eutectic grains and on the Ti-rich regions, respectively. Measurement was according to a standard procedure (ASTM C 1327-15). The hardness was averaged over 20 points.

Table 1. Samples, starting composition, phase assembly in the bulk, Vickers hardness and bending strength, and relative density R of the composites.

Sample	Starting composition (wt. %)			Phase amount in the bulk composites (wt. %)						Vickers hardness, (GPa)		Bending strength, (MPa)	Relative density, R (%)
	B_4C-TiB_2		Ti	B_4C	TiB_2	TiB	Ti	TiC	Ti_2B_5	Eutectic grains	Ti-rich regions		
	B_4C	TiB_2											
SPS20	52	28	20	43	48	-	-	-	5	36±2	22±1.8	237±14	94,8
SPS30	45.5	24.5	30	31	62	-	-	-	4	35±1	21±1.5	300±15	96,2
SPS40	39	21	40	20	73	-	-	-	3	36±2	18±1	285±13	97,8

I35	≈42.5	≈22.5	≈35	38	27	17	13	4	-	35±2	7.9±0,8	220±12	98,9

3. Results and Discussion

3.1 Phase assembly

The XRD patterns are presented in Fig. 2. All samples contain B_4C (PDF 01-075-0424) and TiB_2 (PDF 2002799). Some traces of carbon (PDF 00-026-1080) were also present (less than 2 wt %). The weight percent of the detected phases is listed in Table 1. In the SPSed samples, a small amount of Ti_2B_5 (3-5 wt. %) formed, while in the infiltrated samples, Ti metal (13 wt. %), TiC (4 wt. %) and TiB (17 wt. %) were found. We note that the starting composition in the raw mixtures and the resulting phase assembly in the bulk samples are different. This indicates reactions between the Ti metal and the $(B_4C\text{-}TiB_2)_{eutectic}$ during the processing. As can be observed from Table 1, processing by SPS or infiltration promotes in all samples the occurrence of a higher amount of TiB_2 and a simultaneus decrease in the B_4C amount. The highest enhancement, of more than 3 times, is for sample SPS40 with the highest concentration of Ti in the raw mixture. Authors of refs. [29] reported the following reaction between B_4C and Ti:

$$B_4C + 3Ti \rightarrow 2TiB_2 + TiC \qquad (2)$$

The reaction (2) apparently develops in our samples with the only difference that B_4C is from the $B_4C\text{-}TiB_2$ eutectic grains. However, lack of TiC phase in the XRD patterns for the SPSed samples may indicate the following reaction:

$$B_4C + 2TiC \rightarrow 2TiB_2 + 3C \qquad (3)$$

Reaction (3) needs the presence of TiC previously formed in reaction (2). Therefore, reaction (3) can be considered the later stage of material development. Considering that in the infiltration route the processing is at a lower temperature and for a shorter dwell time than in the SPS, reaction (2) apparently fits the situation of the infiltrated sample where unreacted metallic Ti is available and a low amount of TiC occurs. This may point to a more advanced reaction stage for the SPSed samples than for the infiltrated one, but the SPSed samples also contain another secondary phase, namely Ti_2B_5. According to [30, 31] this phase is the result of a reaction between boron carbide and titanium:

$$3Ti + B_4C \rightarrow 2/3TiB + 2/3Ti_2B_5 + TiC \quad (4).$$

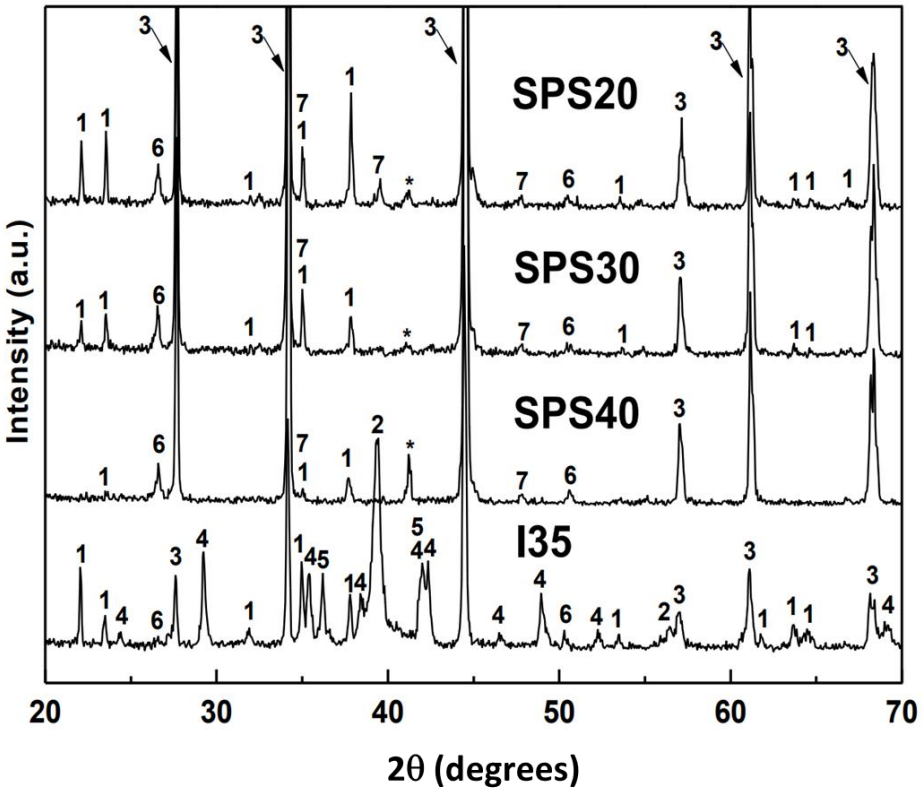

Fig. 2 XRD patterns of ceramics composites with different compositions. Identified phases are: 1 – B_4C (PDF 01-075-0424); 2 – β-Ti (PDF 9012924); 3 – TiB_2 (PDF 2002799); 4 – TiB (PDF 01-079-2942); 5 – TiC (PDF 5910091); 6 – C (PDF 00-026-1080); 7 – Ti_2B_5 (PDF00-066-0528).

Reaction (4) is viewed as an intermediate reaction of the TiB_2 formation in reaction (2), and, hence, it is an early stage reaction. Based on this, one may expect to find the Ti_2B_5 phase in the infiltrated sample, rather than in the SPSed ones. In practice, the situation is opposite and this suggests that kinetic factors and the local availability of Ti around B_4C from the B_4C-TiB_2 eutectic grains has to be taken into consideration, while reaction (4) needs a careful assessment. An extra argument in this direction is that in the SPSed samples in which Ti_2B_5 is present, contrary to expectations from reaction (4), the TiB and TiC phases were not detected by XRD.

The absence of diffraction lines of the metallic Ti in the SPSed samples is mainly explained by reactions (2) and (4), but it can also be the result of the interaction between Ti and residual oxygen from the SPS chamber. The diffraction maximum at 2θ~42 ° (marked with an asterisk in Fig. 2) can be ascribed to Ti (α phase or a phase with dissolved oxygen such as Ti_6O) or to an unidentified impurity phase. The details of the oxygen distribution will be investigated

by microscopy in Section 3.2. The intensity of the peak at 2θ~42 ° is lower in the infiltrated sample, while the peaks of metallic β-Ti are clearly observed in the infiltrated sample. Another specific of the infiltrated sample is the presence of the TiB phase and its relatively high amount of 17 wt. %. This phase may form according to reaction (4) during the early stages of the material development. However, its large amount and lack of Ti_2B_5 in the infiltrated sample questions reaction (4). Considering also the previous paragraph, both the SPS and infiltrated samples suggest the for reconsideration of reaction (4). The large amount of TiB indicates that molten Ti as in the infiltrated sample promotes TiB without Ti_2B_5 formation. In the phase diagrams of Ti-B [32] and Ti-C [33], in the Ti-rich regions (< 2% wt. B or C) the eutectic points are located at 1541 and 1646 ° C. The eutectics are Ti-TiB and Ti-TiC. An XRD analysis (Table 1) shows that in the infiltrated sample, the amount of TiC (4 wt %) is about 4 times lower than the amount of TiB (17 %). This corresponds to a boron to carbon ratio of 4:1 as in the boron carbide. Considering all pieces of information, for the infiltrated sample I35, the following reaction is written:

$$B_4C + Ti \rightarrow 4TiB+TiC \qquad (5)$$

This reaction summarizes the processes in the infiltrated sample where the presented eutectics play an important role and there is no need to consider reaction (4). For the SPSed samples, reaction (4) becomes:

$$7/4B_4C + 3Ti \rightarrow TiB_2 + Ti_2B_5 + 7/4C \qquad (6)$$

Among the reaction products in (3) and (6) is C. Indeed, a small amount of C was detected in the XRD patterns of our SPSed samples, as already presented at the beginning of this section. Carbon can be also added to the material from the graphite die system used during SPS processing.

3.2 Structure by electron microscopy observations

3.2.1 Spark Plasma Sintered samples

The general secondary electron (SE) microscopy images of the SPSed samples SPS 20, 30 and 40 are presented in Figs. 3 (a), (c), and (e), while the backscattering (BS) images are in Figs. 3 (b), (d), and (f). In the backscattering (BS) images, which mainly exhibit a Z-contrast (the brighter the images the higher the atomic number), dark grains with brigher inclusions are the B_4C-TiB_2 eutectic defined as the composite's matrix.

The light-gray macro region in the BS images indicates the presence of a high amount of the heaviest element, i.e., Ti, and represents the reinforcement. The Ti-rich reinforcement shows different nuances of gray suggesting the presence of different Ti-based phases, such as TiB_2,

Ti_2B_5, and Ti(O) detected by XRD. The reinforcement has a composite nature. The structures of the matrix (eutectic grains) and reinforcement (Ti-rich regions) are interpenetrated and have the tendency to form two continuous 3D networks in samples SPS20 and 30, while in the sample SPS40, eutectic grains show some level of isolation in the Ti-rich component. The macrostructure of samples SPS20, 30 and 40 can be considered to be the *bi-continuous* type with each component being a composite. The consequences of the bi-continuous structure on the mechanical properties will be discussed in Section 3.3. SE microscopy images (Fig. 3) also reveal the presence of some

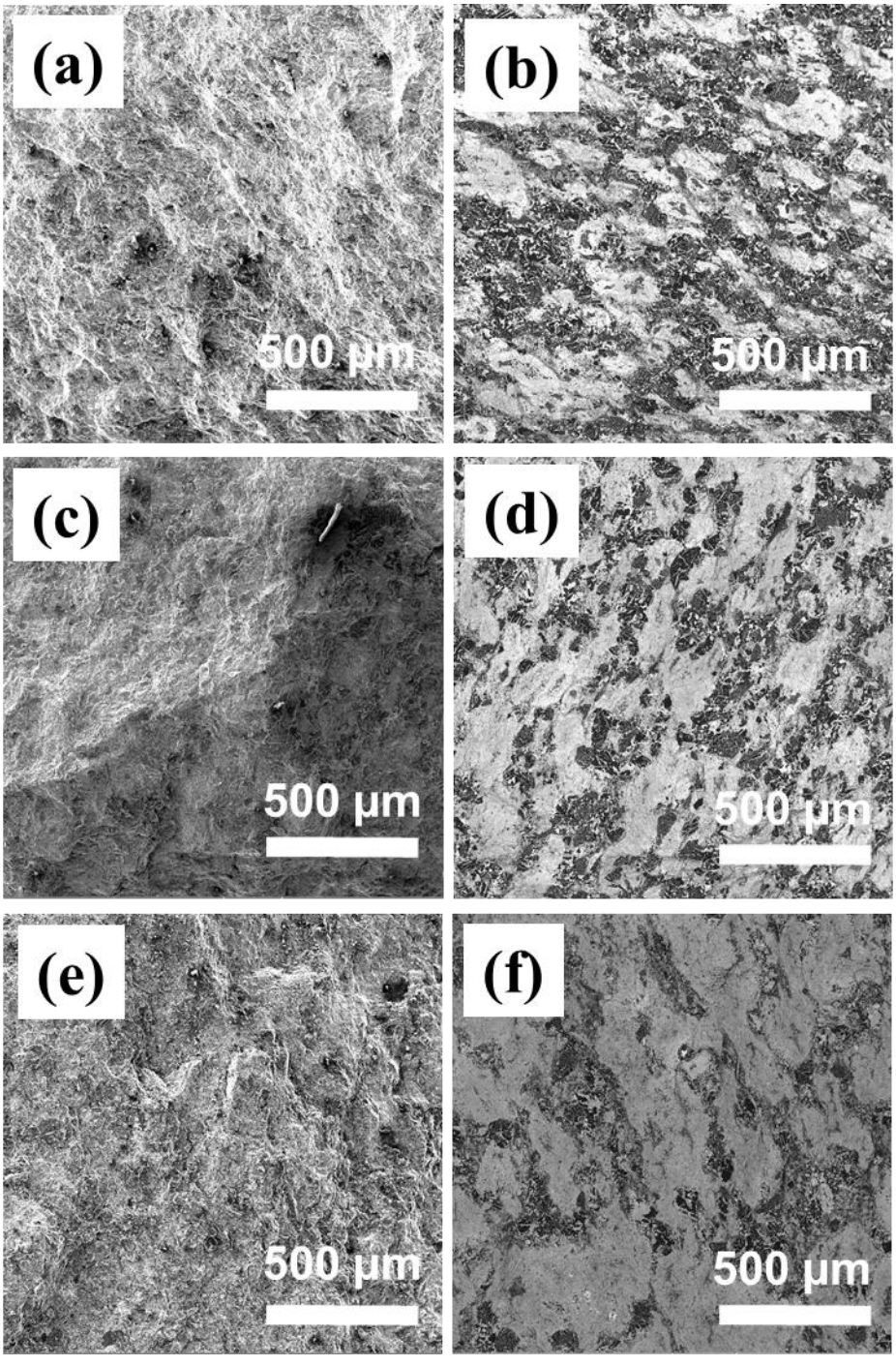

Fig. 3 SEM images on fractured surfaces in secondary electrons (SE) (a, c, e) and backscattering (BS) (b, d, f) modes taken on SPSed samples SPS20 (a, b), 30 (c, d), and 40 (e, f). Samples notation is as in Table 1.

pores in the SPSed samples. More closed pores and smaller are available in the SPS 30 and 40 samples for which the amount of Ti in the starting composition increases and this leads to enhancement of relative density *R* from sample SPS 20 to 30 and to 40 (Table 1). The reason for this behavior is that the addition of the metal decreases the sintering temperature thus improving consolidation of the composite.

Apart from the different mutual distributions of the $(B_4C\text{-}TiB_2)_{eutectic}$ matrix and of the Ti-rich reinforcement, samples SPS 20, 30, and 40 (Fig. 4) show on different grains similar EDS local compositions and examples are presented in Table 2. In the eutectic grains, in most cases, TiB_2-like compositions are detected, while in the Ti-rich reinforcement, two Ti-B compositions are found which are ascribed to phases TiB_2 and Ti_2B_5. These phases were identified in XRD (Fig. 2, Table 1) and their presence supports reaction (6) and discussion from *Section 3.1*. On SEM images, the two Ti-B phases present different gray nuances, but it was not possible to associate a certain phase with a specific gray color because the measured compositions of the two phases are not very different (Table 2). In general, the darker gray Ti-B phase is often isolated in the inner part of the lighter gray Ti-B phase and it has no direct contact with B_4C phase. This is e.g. the case of the needle-like regions marked with yellow elipses and of the grain (2) in Fig. 4 SPS30 (i)). According to EDS (Table 2), the Ti-B phases may contain also some amount of C. Small amounts of impurity elements such as Fe, W, Al, Si or Mn were detected. In general, Al and W follow the Ti distribution from the reinforcement and Fe, Mn and Si are localized at grain boundaries. Oxygen can be at the interface between titanium boride and boron carbide phases (Fig. 4 SPS20 (b), (e), SPS30 (e), SPS40 (b), (e)).

More details are provided by the results of TEM investigations (Fig. 5). There is gradual variation of B and C along the profile line over a boron carbide needle-like area (Fig. 5 (e)). It indicates on diffusion of B and C into Ti with formation of e.g. TiB_2 in Fig. 5 (i) SAED 1). The selected area electron diffraction (Fig. 5 (j) SAED 2) on the boron carbide area show two interplanar distances *d* of 0.212 nm and 0.35 nm. They match the distances for planes (10-2) and (2-13), respectively, of rhombohedral boron (9011036.cif), but the vectorial relationship is not fullfilled. Furthermore, EDS also indicates the presence of carbon. An example of a grain with a B-rich composition, $B_{23.02}CO_{0.04}Fe_{0.002}W_{0.002}$, was measured and it is presented in Fig 1 Supplementary Material. It is noteworthy, that there is a nano layer between TiB_2 and the

depleated B-C phase of about 10 nm in width. Fourier transformed image (Fig 5 (j) FT) indicates a interplanar distance *d* of 0.328 nm. It can be identified with the interplanar distance for the plane (001) (*d* = 0.322 nm) of TiB_2 (9008946.cif) or with (111) (*d* = 3.34 nm) of graphite (1200018.cif). As addressed before, the presence of graphite is in agreement with reaction (6), but a final conclusion cannot be presented. Another aspect of interest is the presence of oxygen at the interface between Ti-B and B-C phases (Fig. 5 (g), (h)). More research is required to establish the details of the interfaces.

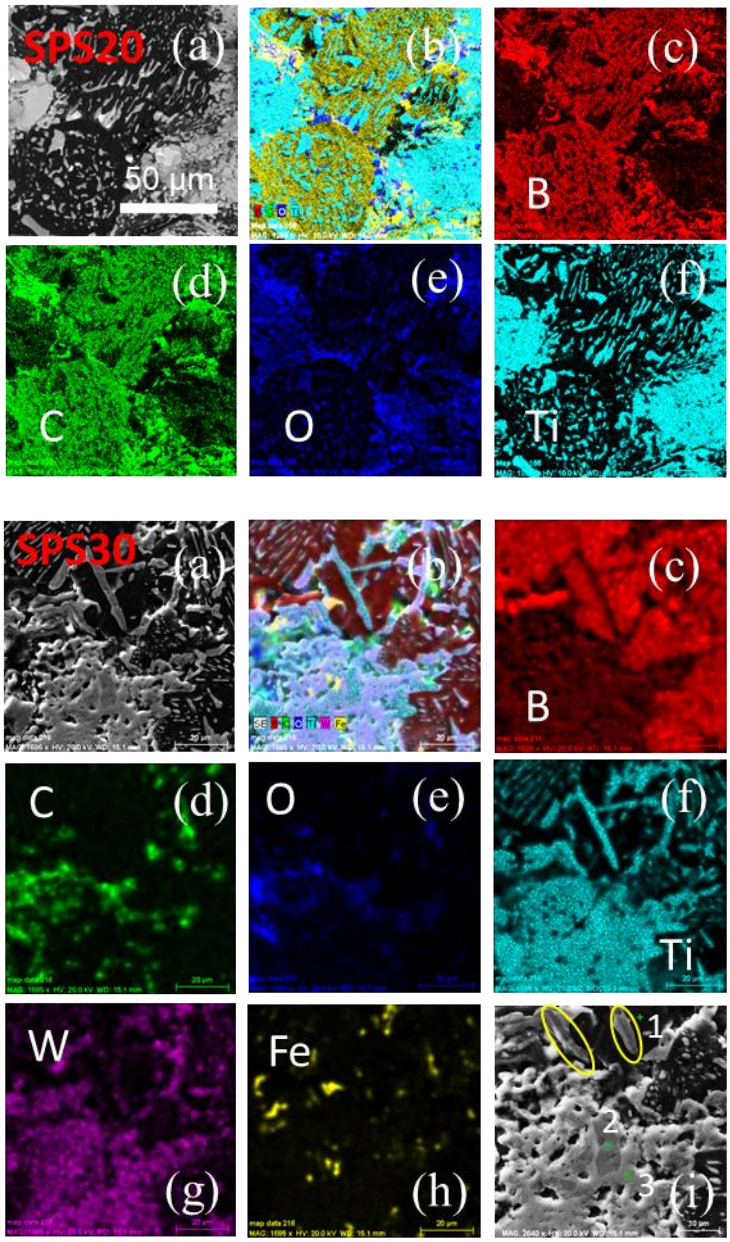

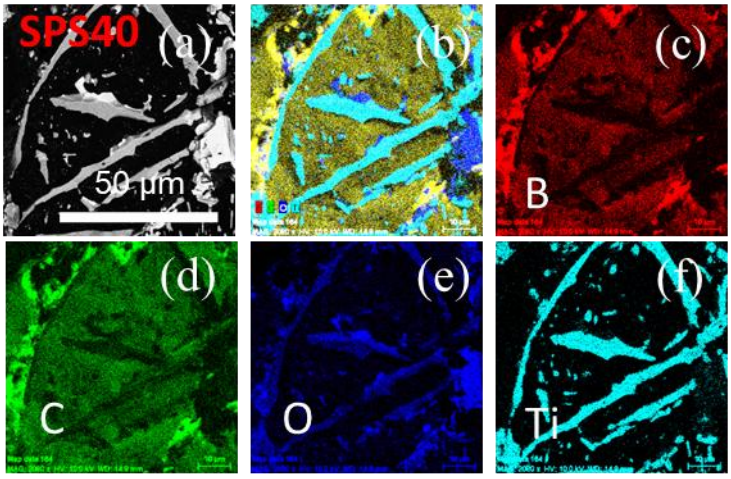

Fig. 4 SEM images and EDS maps for the detected elements. The red-green-blue (RGB) image (SPS20 (b), SPS30 (b), SPS40 (b)) represents the overlapped images for all elements. Samples are: SPS20, 30 and 40. Local EDS compositions (1-3) are gathered in Table 2.

Table 2 EDS local compositions measured on grains from Fig 4 SPS30-(i) and Fig. 7 I35 (i), (j).

Sample	No.	Color in secondary electron regime	EDS stoichiometry Normalized to C or Ti_2	Exp. ratio: B/C	Exp. ratio: Ti/B (Ti/B+C)	Ascribed phase	Theoretical ratio For ascribed phase	Observation
SPS30 (Fig. 4)	1	Black	$B_{4.01}CO_{0.011}Ti_{0.03}Fe_{0.01}$	4.01	-	B_4C	4	-
	2	Dark grey	$Ti_2B_{4.27}C_{0.68}O_{0.068}$	-	0.47 (0.4)	Ti_2B_5 (or TiB_2)	0.4 (0.5)	Ti-B-C
	3	Light gray	$Ti_2B_{3.6}C_{0.67}O_{0.14}$	-	0.55 (0.47)	TiB_2 (or Ti_2B_5)	0.5 (0.4)	Ti-B-C
I35 (Fig. 7)	4	Black	$B_{3.16}CO_{0.006}$	3.16	-	B_4C	4	-
	5	Grey	$Ti_2B_{3.74}C_{0.54}O_{0.185}$	-	0.53 (0.47)	TiB_2	0.5	Ti-B-C
	6	Grey	$Ti_2B_{3.18}C_{2.68}O_{1.01}$	-	0.62 (0.34)	-	-	Ti-phases with B, C and/or O
	7	Intermediate gray	$Ti_2B_{1.14}C_{0.54}O_{0.024}Al_{0.009}Mn_{0.003}$	-	1.75 (1.19)	Ti	-	Ti-B-C Ti-rich
	8	Dark grey	$Ti_2B_{1.98}C_{0.5}O_{0.034}Al_{0.15}Mn_{0.012}$	-	1 (0.81)	TiB	1	Ti-B-C
	9	Light gray	$Ti_2B_{1.07}C_{0.52}O_{0.087}Al_{0.138}Mn_{0.08}$	-	1.86 (1.24)	Ti	-	Ti-B-C Ti-rich

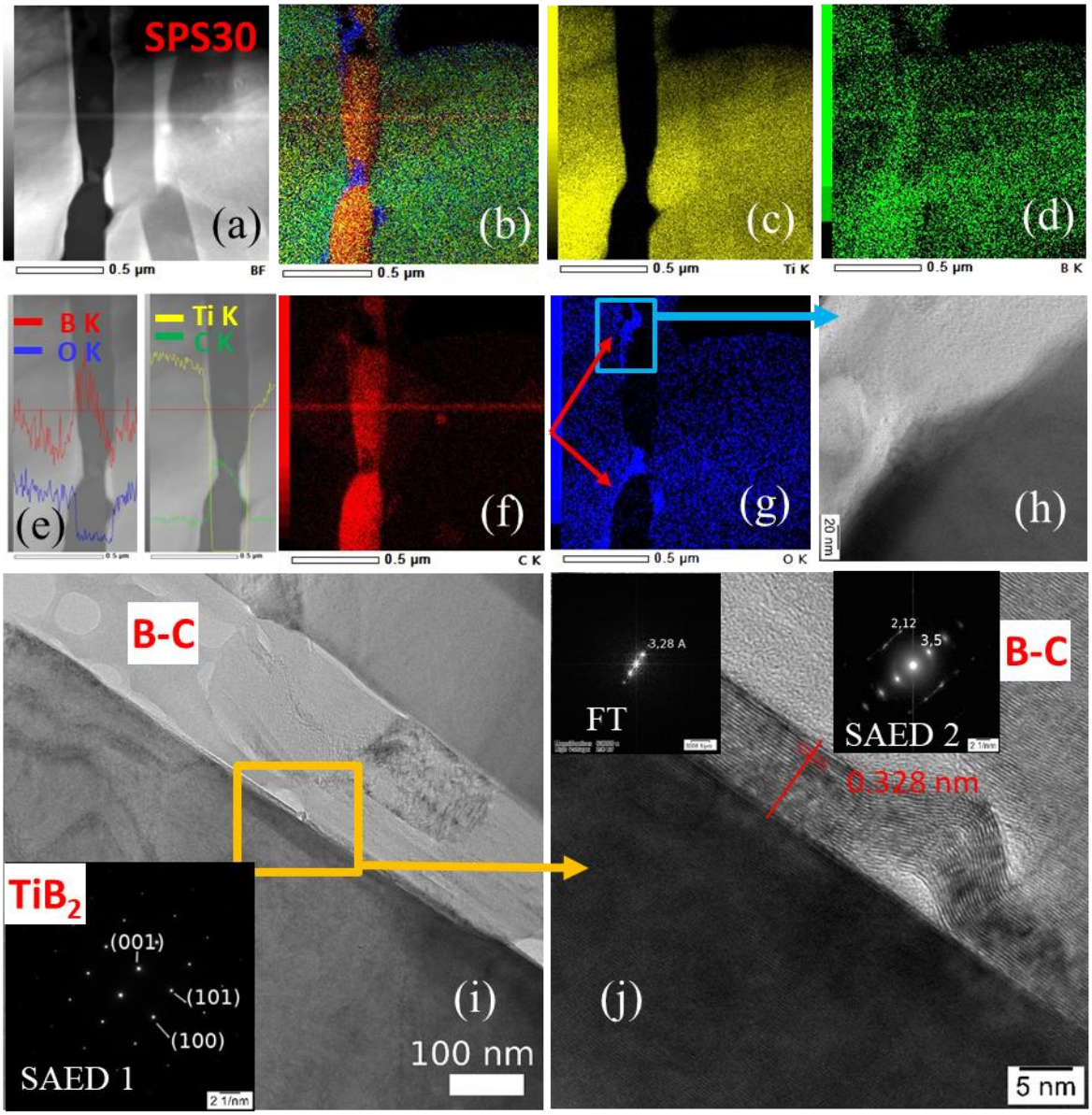

Fig. 5 (a)-(g) - TEM images, EDS elemental maps and profile along indicated line; (h) – TEM image of an oxygen-rich region marked in (g) with red arrows; (i) – TEM image of a Ti-B and B-C interface (inset SAED 1 is selected area electron diffraction of TiB_2); (j) HTEM detail from image (i) showing a nano-layer between TiB_2 and boron carbide (insets are SAED 1 on the depleated boron carbide and Fourier transformed image on the nano layer between TiB_2 and depleated boron carbide).

3.2.2 Infiltrated sample

The macrostructure of the infiltrated sample is presented in Fig. 6. The sample is dense with the highest relative density *R* (Table 1) among the investigated samples.

Eutectic grains are isolated in the Ti-rich component which forms a *3D network*. In this case, a bi-continuous structure is not obtained and the structure is much different from that of the SPSed samples. According to the XRD, sample contains B_4C, TiB_2, βTi, TiC, and TiB. Since the

eutectic grains are composed mainly of B_4C and TiB_2, the Ti-rich reinforcement is a composite. Indeed, Fig. 7 indicates that Ti-rich region is made of TiB and Ti-rich phases (Table 2) containing C, O and possibly impurity elements (found also in the SPS samples). TEM confirms Ti-rich phase (e.g. $Ti_2BC_{0.14}O_{0.016}$; Fig 2 Supplementary Material) and a gradual variation of Ti (Fig. 8). With the increase of the Ti/B ratio, in SEM images the color of the Ti-containing grains from the Ti-rich reinforcement changes from dark to light gray (Table 2, see EDS No 8, 7, 9 and Fig. 7 (j)). Due to small amount (3 wt. %, Table 1) we could not identify and observe by TEM the morphology of TiC. Nevertheless, according to SEM/EDS observation, in the Ti-rich reinforcement, close to its interface with B_4C-TiB_2 eutectic grains, some regions are O and C rich (Fig. 7 I35 (d), (e), (i); Table 2, EDS No. 6).

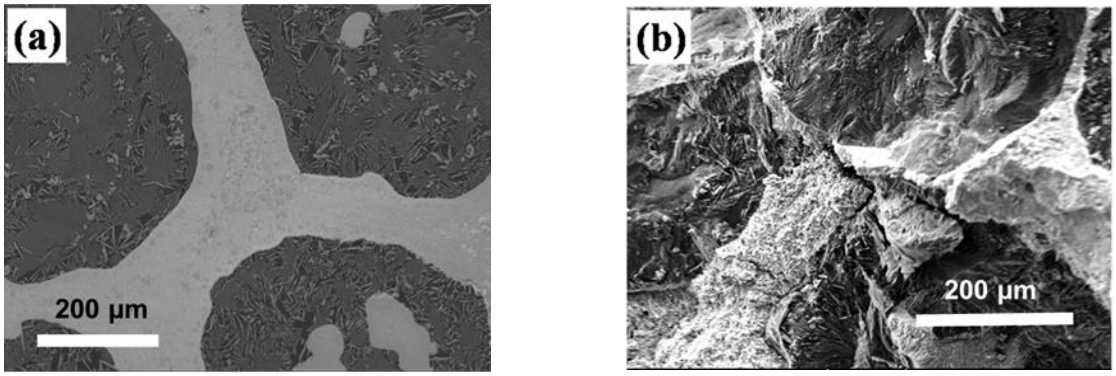

Fig. 6 SEM images of the infiltrated sample: (a) – polished surface; (b) – fractured surface.

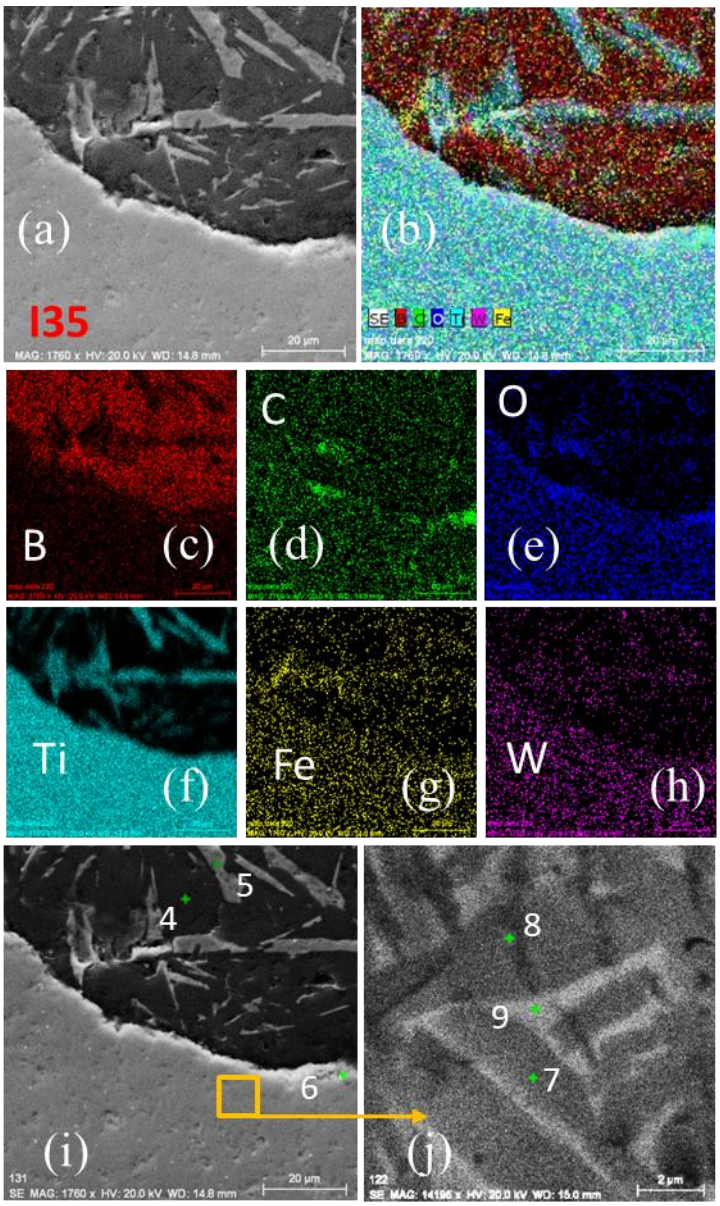

Fig. 7 (a), (c) – (h) - SEM image and EDS maps for the detected elements; (b) - The red-green-blue (RGB) image represents the overlapped images for all elements; (i) and (j) are SEM images where (j) is the square region from (i) at high magnification on Ti-rich region. Local EDS compositions (4-9) are presented in Table 2. Sample is I35.

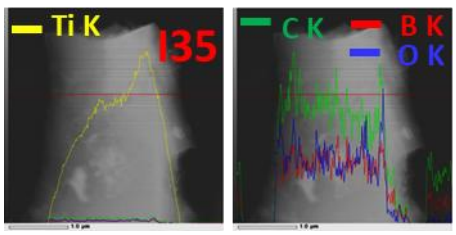

Fig. 8 TEM image of a Ti-rich grain in sample I35 and EDS elemental profile along the indicated line.

In summary, this section reveals that materials from this study are complex hierarchical composites. SPSed samples are *bi-continuous type ceramic composites*, while the infiltrated sample is a *3D metal-like network composite* with isolated ceramic (eutectic) particles. Expectations are that the mechanical properties of the sintered and infiltrated samples are significantly different. However, in the view of presented information regarding phases and interfaces, SEM images in Fig. 9 reveal a strong bonding between the eutectic grains (matrix) and the Ti-rich 3D component (reinforcement) for both the SPSed and infiltrated samples. The interface is a composite. Since the highest enhancement in the amount of the newly formed phases during reactive processing is for TiB_2 in the SPSed samples and for TiB for the infiltrated samples, these phases are the most probable bonding elements between the eutectic matrix and the Ti-rich reiforcement. Other possible phases at the interface are Ti_2B_5 in the SPSed samples and TiC in the infiltrated sample. At the interface, oxygen and carbon (in the Ti-B phases or as graphite) also participate. The source of oxygen is the residual oxygen from the SPS chamber and oxygen from the raw powders. Oxygen is mostly found to be located at grain boundaries (Figs. 4, 5, 7). Considering the variation in the intensity of the color in the EDS map, the amount of oxygen likely changes at different locations. Further work is needed to assess the state of oxygen in our materials.

A gradual change in composition at the interface between two different phases is possible as a consequence of interdiffusion. Some impurity elements were detected in our samples.

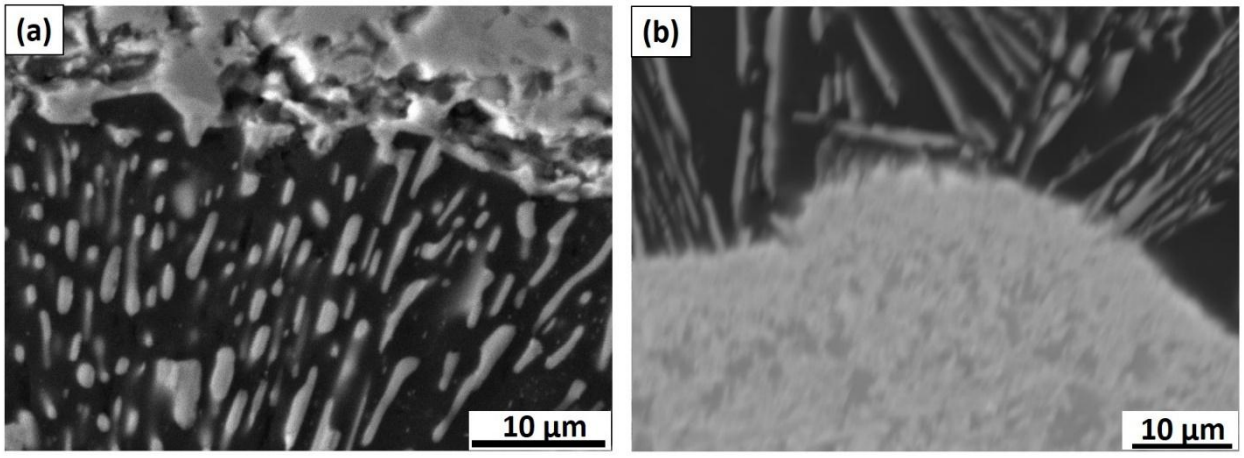

Fig. 9 SEM images of the interface between B_4C-TiB_2 eutectic grains and Ti-rich matrix: (a)- SPSed sample SPS 30 and (b)- infiltrated I35.

3.3 Mechanical properties and fractography analysis

Indentations were performed on the Ti-rich component (reinforcement) and on the eutectic $(B_4C\text{-}TiB_2)_{eutectic}$ grains (of the matrix).

The average values of the Vickers hardness (HV) for the different SPSed samples were 35-36 GPa on the eutectic grains, and 18-22 GPa on the Ti-rich component (Table 1, SPS samples). The values measured on the eutectic grains correspond to those reported for the B_4C-TiB_2 eutectic crystals [5, 6]. As already addressed, the main phase in the Ti-rich reinforcement macroregion of the composite is TiB_2. Its hardness according to [11] is 21-23 GPa. The values match those measured on the Ti-rich component of our SPSed composites. Hence, the composite is of a ceramic-ceramic type, i.e., it is mainly brittle, but hard. Indeed, for samples SPS 30 and 40, one observes in Fig. 10 that the indentation produced long cracks. Cracks show deflection and bridging depending on the presence, location and distribution of the harder grains such as B_4C-TiB_2. Cracks are not linear and they show a teeth-saw-like pattern. This provides a certain level of plasticity to the system; the fracture mode is mainly intragranular, typical for hard and brittle materials, but the intergranular mechanism is also active and it promotes improvement of the fracture toughness. The intergranular fracture may be contributed by Ti oxide and graphite softer phases located at grain boundaries between boride or carbide hard phases. Some influence is also expected from impurity elements when available at grain boundaries. Cracks are developing from the corners of the indentation trace (Fig. 10, SPS 40) when an indentation is performed on the Ti-rich region. The close proximity of the harder eutectic grains to the indent (Fig. 10, SPS 30, regions with green circles) can lead to initiation of cracks from other locations, e.g., from the points on the indent side. These cracks are running perpendicular to the indent-trace side. Eutectic grains arrest the cracks, but the situation is complex. A closer look at the fractured surface reveals that:

(i) the surface roughness of the Ti-rich region is higher than for the eutectic grains (Fig. 11a). This is as expected and confirms that the hardness of the Ti-rich component is lower than for the former eutectic one.

(ii) Remarkable is that an intergranular micro ‘pull out’ mechanism of the grains at the Ti-rich – eutectic interface is observed (Figs. 11 a-d, follow the yellow ovals in the (a) and (c) images). This mechanism was also revealed in the SPSed samples prepared only from the eutectic B_4C-TiB_2 grains without additives [7]. The grains that are pulled out are TiB_2 inclusions from the B_4C-TiB_2 eutectic. Special for the samples from this study is that this mechanism occurs at the interface between the Ti-rich region and the B_4C-TiB_2 eutectic grain. It suggests differential bonding strength between the Ti-rich – B_4C and Ti-rich – TiB_2. In particular, the bonding between the Ti-rich and TiB_2 seems very strong since it can overcome the bonding between B_4C

and TiB_2 in the eutectic grain. As presented in Sections 3.1 and 3.2.1 the Ti-rich region is composed of TiB_2, but also of Ti_2B_5. A higher relative amount of B in Ti_2B_5 than in TiB_2 (Ti_2B_4) can provide a higher hardness to Ti_2B_5, but authors are not aware of any study reporting the hardness of Ti_2B_5. The 'pull out' intergranular mechanism at the interface between Ti-rich and B_4C-TiB_2 or between the B_4C and TiB_2 of the eutectic grain enhances the plasticity of the composite in the fracturing process.

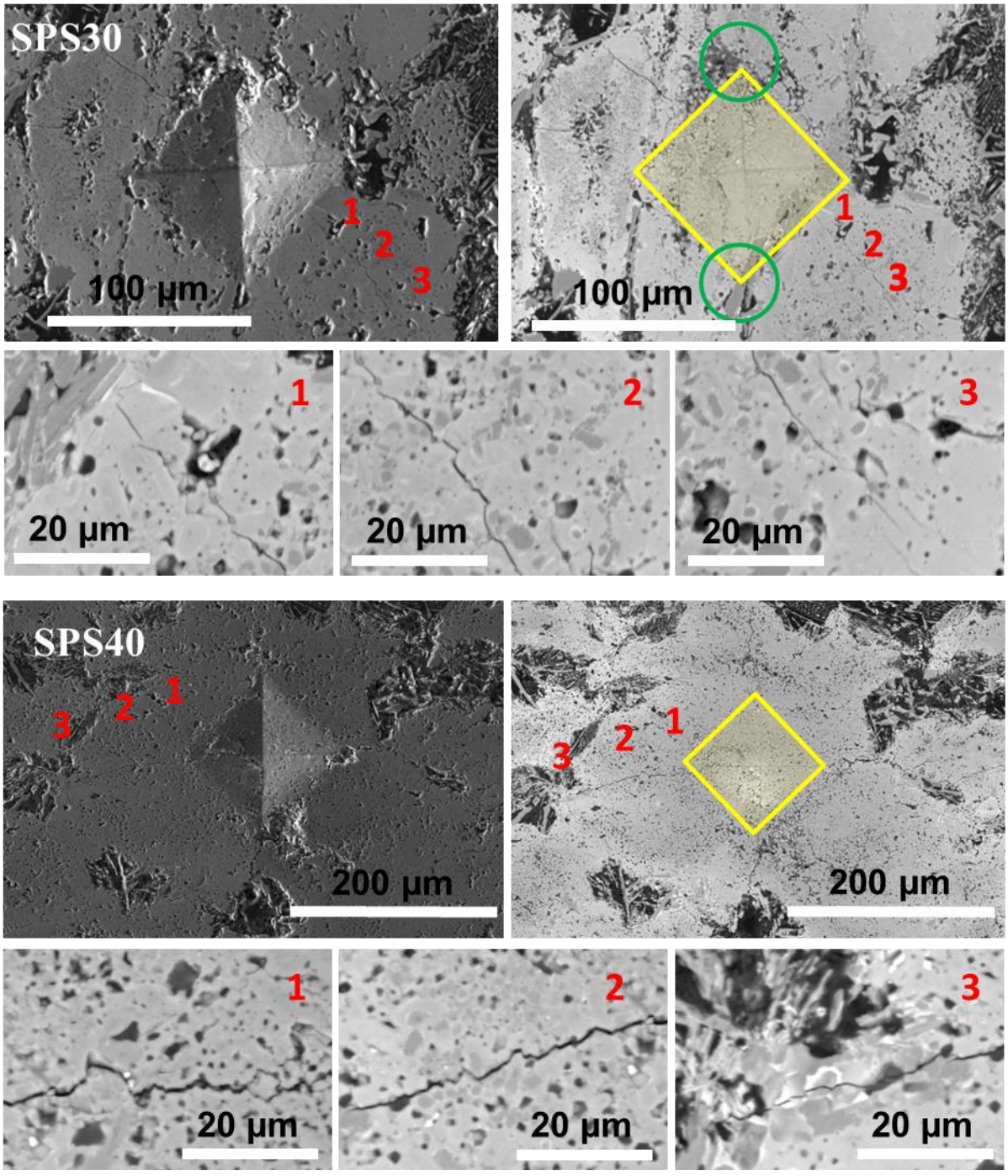

Fig. 10 SEM images showing indentation traces and details of the cracks for samples SPS 30 and 40.

Results of the three-point bending tests at room temperature are presented in Fig. 12. Although the strength-displacement curves are linear denoting a typical brittle behavior as already inferred from the indentation measurement, the already presented toughening mechanisms

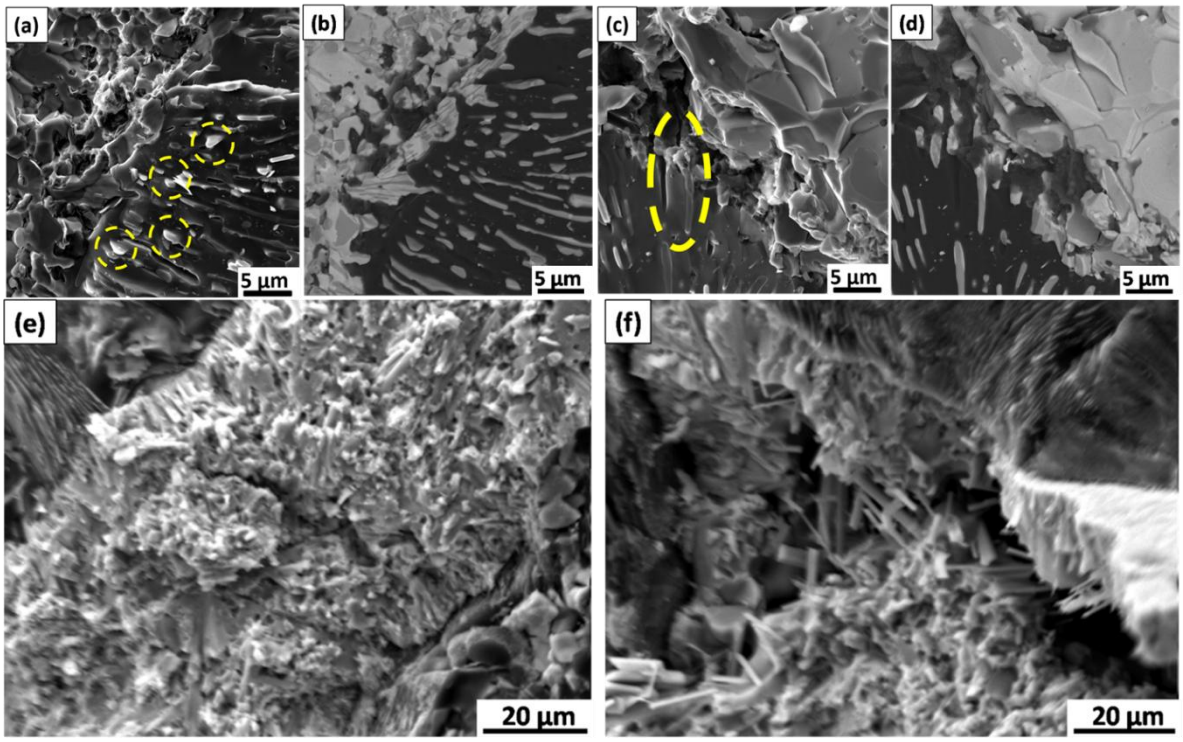

Fig. 11 SEM images of fracture surface of: SPSed sample (SPS30) in SE mode (a, c) and in SE mode (b, d); infiltrated sample in SE mode (e, f). Yellow circle/ellipse indicate regions where Ti-B grains are pulled out.

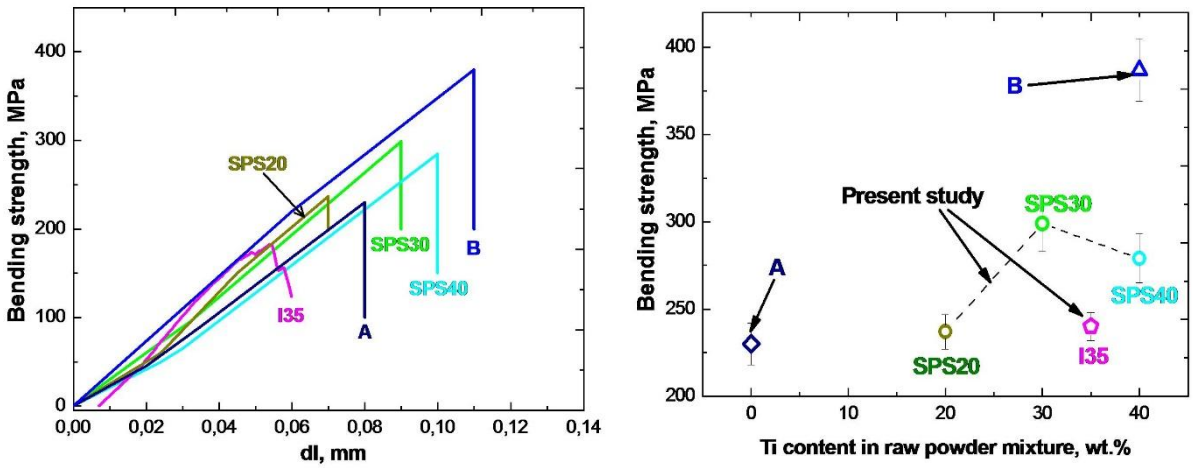

(a) (b)

Fig. 12 Stress–displacement curves (a) and the maximum bending strength with Ti amount for samples A [7], B [6], SPS 20, 30, 40, and I35; Sample A and B were obtained by SPS from a

B_4C-TiB_2 eutectic powder and from a mixture of powders with starting composition (60 wt% B_4C + 40 wt% $(B_4C\text{-}TiB_2)_{eutectic}$), respectively.

contribute to the displacement until failure under a bending load and, with the increase in the Ti content from 20 to 40 wt.% for the SPSed sample, the displacement continuously increases (Fig. 12a). The meaning of this result is that the fracture toughness enhances with the added Ti amount. From the viewpoint of a 'two-component' macrostructure and of its impact on the fracture toughness, our result roughly resembles the situation presented in ref. [34]. Namely, the fracture toughness of an Al_2O_3 composite reinforced with 0, 10, 30 and 50 wt% Fe fabricated by PM increases with a higher amount of Fe. Beyond 30-50 wt.% of Fe, it decreases. While the similarity may be considered straightforward, the complex nature of the toughening mechanism from our composites should not be neglecled. However, to understand the share contribution of each mechanism depending on hierarchical structure of our composite on the mechanical properties details, more research is needed. Of much interest is also that not only the toughness increases, but also the bending strength improves with the Ti addition. The values of the bending strength in the Ti-free reference sample A [7] and in the Ti-added samples SPS 20, 30 and 40 show a maximum of 300 MPa for the optimum sample SPS30. Different factors (phases, pores, interfaces, hierachical structure) as in the case of the fracture toughness contribute to the bending strength result. The addition of Ti to a B_4C-TiB_2 eutectic ceramic is at the origin of a non trivial mechanical behavior. Additional possible arguments supporting this idea is that the displacement for sample A does not fit the tendency observed for samples SPS 20, 30 and 40 (displacement for sample A is between those for samples SPS 20 and SPS 30), while both the displacement and bending strength are the highest in reference sample B [5] with the starting composition (60 wt% B_4C + 40 wt% $(B_4C\text{-}TiB_2)_{eutectic}$) (Fig. 12b). Nevertheless, it is noteworthy that the direct comparison between the samples from this study and samples A and B is not possible since the SPS processing parameters were not identical and eutectic particles in the reference samples are directionally solidified in a floating zone growth meaning that the 1D TiB_2 inclusions have a preferential orientation in a B_4C single-crystal-like particle.

As already mentioned, in the SPSed samples 20-40, the presence of a small amount of graphite and of Ti oxides can also have a positive impact on toughening through the intergranular fracturing mechanism. Toughening improvement can be also provided by the gradual changes in the composition at grain boundaries.

The hardness of the Ti-rich macrocomponent from the infiltrated sample I35 is about 8 GPa (Table 1). This value is about three or four times higher than for the pure titanium (2-2.6

GPa for βTi [35]). It is also about two times higher than for the Ti-TiB composites [36]. The result suggests a strengthening effect of the Ti-rich component of our composite by the presence of ceramic TiB, TiC, and $(B_4C\text{-}TiB_2)_{eutectic}$. We remind that in the infiltrated sample, Ti metal is present in the Ti-rich 3D network-like region. Hence, sample I35 should present a strong ductile behavior. Indeed, in Fig. 11 (e) the Ti-rich region shows high roughness as for surfaces resulting from plastic fracturing. Indentation does not produce long cracks (Fig. 13, follow the yellow, full line arrows) as for the sintered samples. This indicates high fracture toughness values. Crack propagation is impeded not only by the metallic–type fracture of the Ti-rich region, but it can be deflected or arrested by

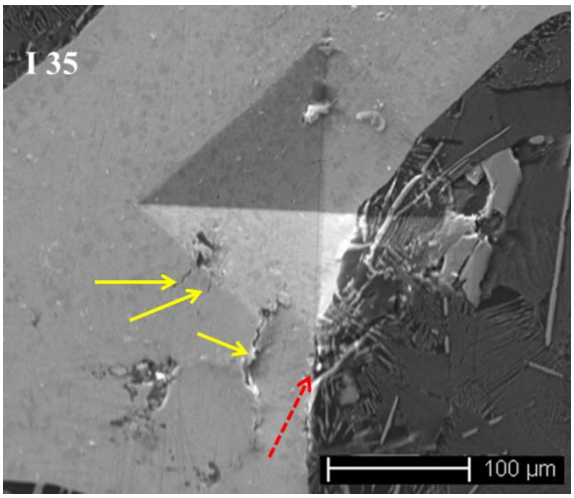

Fig. 13 SEM image taken on the indentation trace from the surface of the infiltrated I35 composite sample. Yellow full-line arrows indicate cracks in the Ti-rich ductile region. The red dashed-line arrow shows the crack parallel to the interface between Ti-rich region and the $(B_4C–TiB_2)_{eutectic}$ particle.

the eutectic hard grains. Deflection occurs along the interface between the Ti-rich and $B_4C\text{-}TiB_2$ (Fig. 13, follow the red, dashed-line arrow). To have this situation, the crack arriving at the interface should be as close as possible to the tangent of the $B_4C\text{-}TiB_2$ eutectic grain. When the crack is closer to normal to the interface, it is arrested. As for the SPSed samples, at the interface there is an active "pull out" intergranular mechanism; individual 1D objects or packages of these elements (sometimes parallel), usually containing Ti and B, can be observed at the fractured interface in Figs. 11 (e), (f). Close to ultimate fracturing, in the strength-displacement curves for the bending load at room temperature, multiple steps occur (Fig. 12 (a), I35). A similar curve departing from the typical linear dependence of brittle materials and with a multistep shape was reported in ref [37] for a particle reinforced metal-matrix SiCp-

6061Al/6061Al composite. This composite has the fracture toughness close to the level for an unreinforced 6000 series aluminum alloy. The explanation and the proposed mechanism from ref. [37] can be adapted for the I35 sample. The distinct stages of the fracture process are induced by the fact that in plastic materials the main crack nucleation and growth are not instantaneous and, thus, the composite does not fracture completely. Namely, there is plastic deformation that absorbs fracture energy so that the crack is obstructed and propagates along the metal-ceramic interface in the first composite layer (with eutectic grains in our case) closest to the notch or surface flaw. For I35 material, the crack propagation along the metal-ceramic interface is influenced by bridging/anchoring through the pull out mechanisms: (i) the *micro pull out* mainly of the 1D Ti-B grains and by the *macro-pull out* of the eutectic grains from the Ti-rich ductile component (Fig. 6 (b), Fig. 11 (f)). The external load must increase to overcome bridging from the first layer, to further deform the metal (Ti-rich region in our case) and to make the crack to propagate until the second layer with eutectic particles fractures. The indicated stages will repeat until the fracture is complete and material's integrity is destroyed. It results that the high fracture performance of I35 is due to plastic deformation of the ductile Ti-rich composite and to debonding specific features at the interface between Ti-rich composite and eutectic grains.

Remarkable is that although the sample is ductile, it shows a bending strength similar (Fig. 12 (b), Table 1) to that for the brittle samples A-reference and SPS20.

4. Conclusion

Powders of $(B_4C–TiB_2)_{eutectic}$ grains reinforced with Ti were processed by two routes, namely, spark plasma sintering and infiltration. Complex novel hierarchical composites were obtained. SPSed samples are bi-continuous type ceramic composites, while the infiltrated sample is a 3D metal-like network composite with isolated ceramic (eutectic) particles.

Spark plasma sintered composites are composed of ceramic phases and show a brittle behavior with a continuous enhancement of the bending displacement when the Ti amount increases from 20 to 30 and 40 wt. %, while the bending strength shows a maximum of 300 MPa for the sample with 30 wt. % Ti. The maximum bending strength is higher than for a reference sample A, SPSed from the eutectic particles. In the SPSed composites from this study, strengthening and toughening simultaneously occur when the Ti amount is up to about 30 wt. %.

The infiltrated sample contains Ti metal and is ductile, while the bending strength is comparable to the values for brittle SPSed reference sample A produced from the eutectic

particles and for the sample added with 20 wt. % Ti. Toughening and strengthening mechanisms involve intragranular and intergranular fracturing mechanisms that are active at the micro and macro levels.

Both the SPSed and infiltrated materials present a local specific pull-out mechanism involving mainly Ti-B 1D-grains at the interface between the Ti-rich and $(B_4C–TiB_2)_{eutectic}$ macrocomponents. The bonding between macro components is strong.

Our results indicate that boride or boride-carbide eutectic systems reinforced with metals, preferably lightweight, are of interest for further research and applications given that a complex optimization is undertaken and key factors controlling the desired mechanical properties are revealed. This effort may provide properties that are not available for conventional composites. In the novel complex hierarchical composites from this study, the micro and macro "pull out" mechanisms involving Ti-B 1D objects and $B_4C–TiB_2$ eutectic grains, respectively, contribute to a bridging/anchoring effect that enhances the strengthening and toughening processes.

Acknowledgements

I.S. acknowledges NIMS internship fellowship and Ministry of Education and Science of Ukraine project No 0117U006427. P.B. and A.K. acknowledge UEFISCDI project POC 37_697 no. 28/01.09.2016 REBMAT and Core Program PN19-03 (contract no. 21 N/08.02.2019) Romania.

References

1. K. Lu, The future of metals, Science 328 (2010) 319-320. https://DOI:10.1126/science.1185866
2. L.J. Huang, L. Geng, H.-X. Peng, Microstructurally inhomogeneous composites: is a homogeneous reinforcement distribution optimal? Prog. Mater. Sci. 71 (2015) 93-168. https://doi.org/10.1016/j.pmatsci.2015.01.002
3. J. Lorca, V.M. Orera, Directionally solidified eutectic ceramic oxides, Progress in Materials Science 51 (2006) 711–809. https://doi.org/10.1016/j.pmatsci.2005.10.002
4. P.B. Oliete, J.I. Peña, A. Larrea, Ultra-high-strength nano-fibrillar Al_2O_3–YAG–YSZ eutectics, Adv. Mater. 19 (2007) 2313–2318. https://doi.org/10.1002/adma.200602379
5. I. Bogomol, P. Badica, Y. Shen, T. Nishimura, P. Loboda, O. Vasylkiv, Room and high temperature toughening in directionally solidified $B_4C–TiB_2$ eutectic composites by Si doping, J. Alloys Compd. 570 (2013) 94-99. https://doi.org/10.1016/j.jallcom.2013.03.084

6. I. Bogomol, H. Borodianska, T. Zhao, T. Nishimura, Y. Sakka, P. Loboda, and O. Vasylkiv, A dense and tough (B_4C–TiB_2)–B_4C ‘composite within a composite’produced by spark plasma sintering, Scr. Mater. 71 (2014) 17-20. https://doi.org/10.1016/j.scriptamat.2013.09.022
7. I. Bogomol, S. Grasso, T. Nishimura, Y. Sakka, P. Loboda, O. Vasylkiv, Hard polycrystalline eutectic composite prepared by spark plasma sintering, Ceram. Int. 38 (5) (2012) 3947-3953. https://doi.org/10.1016/j.ceramint.2012.01.048
8. R.L. Ashbrook, Directionally Solidified ceramic eutectics, J. Am. Ceram. Soc. 60 (1977) 428-435. https://doi.org/10.1111/j.1151-2916.1977.tb15527.x
9. F. Trevenot, Boron carbide – a comprehensive review, J. Eur. Ceram. Soc. 6 (1990) 205–225. https://doi.org/10.1016/0955-2219(90)90048-K
10. W.-T. Chen, R. M. White, T. Goto, E. C. Dickey, Directionally solidified boride and carbide eutectic ceramics, J. Am. Ceram. Soc. 99 (2016) 1837–1851. https://doi.org/10.1111/jace.14287
11. I. Gunjishima, T. Akashi, and T. Goto, Characterization of directionally solidified B_4C-TiB_2 composites prepared by a floating zone method, Mater. Trans. 43[4] (2002) 712–720. https://doi.org/10.4028/www.scientific.net/KEM.247.209
12. K.B. Panda, K.S. Ravi Chandran, Synthesis of ductile titanium–titanium boride (Ti–TiB) composites with a beta-titanium matrix: the nature of TiB formation and composite properties, Metal Mater. Trans. A 34 (2003) 1371–85. https://doi.org/10.1007/s11661-003-0249-z
13. D. Demirskyi, H. Borodianska, Y. Sakka, O. Vasylkiv, Ultra-high elevated temperature strength of TiB_2-based ceramics consolidated by spark plasma sintering, J. Euro. Ceram. Soc. 37 (2017) 393-397. https://doi.org/10.1016/j.jeurceramsoc.2016.08.009
14. D. Dudina, D. Hulbert, D. Jiang, D. Unuvar, S.J. Cytron, A.K. Mukherjee, In situ boron carbide–titanium diboride composites prepared by mechanical milling and subsequent spark plasma sintering, J. Mater. Sci. 43 (2008) 3569-3576. https://doi.org/10.1007/s10853-008-2563-8
15. M.W. Barsoum, B. Houng, Transient plastic phase processing of titanium-boron-carbon composites, J. Am. Ceram. Soc. 76 (1993) 1445-1451. https://doi.org/10.1111/j.1151-2916.1993.tb03924.x
16. D. Brodkin, S. Kalidindi, M. Barsoum, A. Zavaliangos, Microstructural evaluation during transient plastic processing of titanium carbide-titanium boride composites, J. Am. Ceram. Soc. 79 (1996) 1945-1952. https://doi.org/10.1111/j.1151-2916.1996.tb08017.x
17. M.W. Barsoum, B. Houng, Transient plastic phase processing of titanium-boron-carbon composites, J. Am. Ceram. Soc. 76 (1993) 1445-1451. https://doi.org/10.1111/j.1151-2916.1993.tb03924.x
18. F. Hong, M.H. Lewis, Ceramic-matrix composites via in-situ reaction sintering, Ceram. Eng. Sci. Proc. 14 (1993) 699-706. https://doi.org/10.1002/9780470314234.ch2
19. V.V. Patel, A. El-Desouky, J.E. Garay, K. Morsi, Pressure-less and current-activated pressure-assisted sintering of titanium dual matrix composites: effect of reinforcement particle size, Mater. Sci. Eng. A 507 (2009)161–166. https://doi.org/10.1016/j.msea.2008.11.046

20. S.C. Tjong, Y.W. Mai, Processing-structure-property aspects of particulate- and whisker-reinforced titanium matrix composites, Compos. Sci. Technol. 68 (2008) 583–601. https://doi.org/10.1016/j.compscitech.2007.07.016
21. K. Morsi, V. Patel, Processing and properties of titanium–titanium boride (TiB_w) matrix composites – a review, J. Mater. Sci. 42 (2007) 2037–47. https://doi.org/10.1007/s10853-006-0776-2
22. Z.Y. Ma, S.C Tjong., L. Gen, In-situ Ti–TiB metal-matrix composite prepared by a reactive pressing process, Scr. Mater. 42 (2000) 367–373. https://doi:10.1016/S1359-6462(99)00354-1
23. W.J. Lu, D. Zhang, X.N. Zhang, R.J. Wu, T. Sakata, H. Mori, Microstructure and tensile properties of in situ (TiB+TiC)/Ti6242 (TiB:TiC=1:1) composites prepared by common casting technique, Mater. Sci. Eng. A 311 (2001) 142–150. https://doi.org/10.1016/S0921-5093(01)00910-8
24. K. Morsi, V.V. Patel, S. Naraghi, J.E. Garay, Processing of titanium-titanium boride dual matrix composites, J. Mater. Process. Technol. 196 (2008) 236–242. https://doi.org/10.1016/j.jmatprotec.2007.05.047
25. B.X. Liu, L.J. Huang, L. Geng, B. Wang, X.P. Cui, C. Liu, G. Wang, Microstructure and tensile behavior of novel laminated Ti–TiB_w/Ti matrix composite by reaction hot pressing, Mater. Sci. Eng. A 583 (2013) 182–187. https://doi.org/10.1016/j.msea.2013.06.058
26. L.J. Huang, S. Wang, Y.S. Dong, Y.Z. Zhang, F. Pan, L. Geng, H.X. Peng, Tailoring a novel network reinforcement architecture exploiting superior tensile properties of in situ TiBw/Ti composites, Mater. Sci. Eng. A 545 (2012) 187–193. https://doi.org/10.1016/j.msea.2012.03.019
27. P.I. Loboda, T.O. Soloviova, Y.I. Bogomol, D.J. Remizov, O.I. Bilyi, Effect of the crystallization kinetic parameters on the structure and properties of a eutectic alloy of the LaB_6–TiB_2 system, J. Superhard Mater. 37 (2015) 394–404. https://doi.org/10.3103/S1063457615060040
28. G.W. Marks and L.A. Monson, Effect of certain group IV oxides on dielectric constant and dissipation factor of barium titanate, Ind. Eng. Chem. 47 (1955) 1611–20. https://doi.org/10.1021/ie50548a044
29. H. Zhao, Y.-B. Cheng, Formation of TiB_2-TiC composites by reactive sintering, Ceram. Int. 25 (1999) 353-358. https://doi.org/10.1016/S0272-8842(98)00048-0
30. M.W. Barsoum, B. Houng, Transient plastic phase processing of titanium-boron-carbon composites, J. Am. Ceram. Soc. 76 (1993) 1445-1451. https://doi.org/10.1111/j.1151-2916.1993.tb03924.x
31. K. Morsi, V.V. Patel, Processing and properties of titanium-titanium boride (TiB_w) matrix composites: a review, J. Mater. Sci. 42 (2007) 2037-47. https://doi.org/10.1007/s10853-006-0776-2
32. E. Rudy, Ternary phase equilibria in transition metal-boron-carbon-silicon systems, Tech. Rep. No AFML-TR-65-2 Part II., Volume VIII. 1966.
33. L.F.S. Dumitrescu, M. Hillert, B. A. Sundman, Reassessment of Ti-C-N based on a critical review of available assessments of Ti-N and Ti-C, Zeitschrift für Metallkunde 90 (1999) 534-541.

34. K. Konopka, A. Olszojwka-Myalska, M. Szafran, Ceramic-metal composites with an interpenetrating network, Mater. Chem. Phys. 81 (2003) 329–332. https://doi.org/10.1016/S0254-0584(02)00595-3
35. Y.L. Kao, G.C. Tu, C.A. Huang, T.T. Liu, A study on the hardness variation of α- and β-pure titanium with different grain sizes, Mater. Sci. Eng. A 398 (2005) 93–98. https://doi.org/10.1016/j.msea.2005.03.004
36. H. Attar, M. Bönisch, M. Calin, L. C. Zhang, K. Zhuravleva, A. Funk, J. Eckert, Comparative study of microstructures and mechanical properties of in situ Ti–TiB composites produced by selective laser melting, powder metallurgy, and casting technologies, J. Mater. Res. 29 (2014) 1941–1950. https://doi.org/10.1557/jmr.2014.122
37. S. Qin, G. Zhang, Preparation of high fracture performance SiCp-6061A1/6061A1 composite, Materials Science and Engineering A279 (2000) 231–236. https://doi.org/10.1016/S0921-5093(99)00627-9

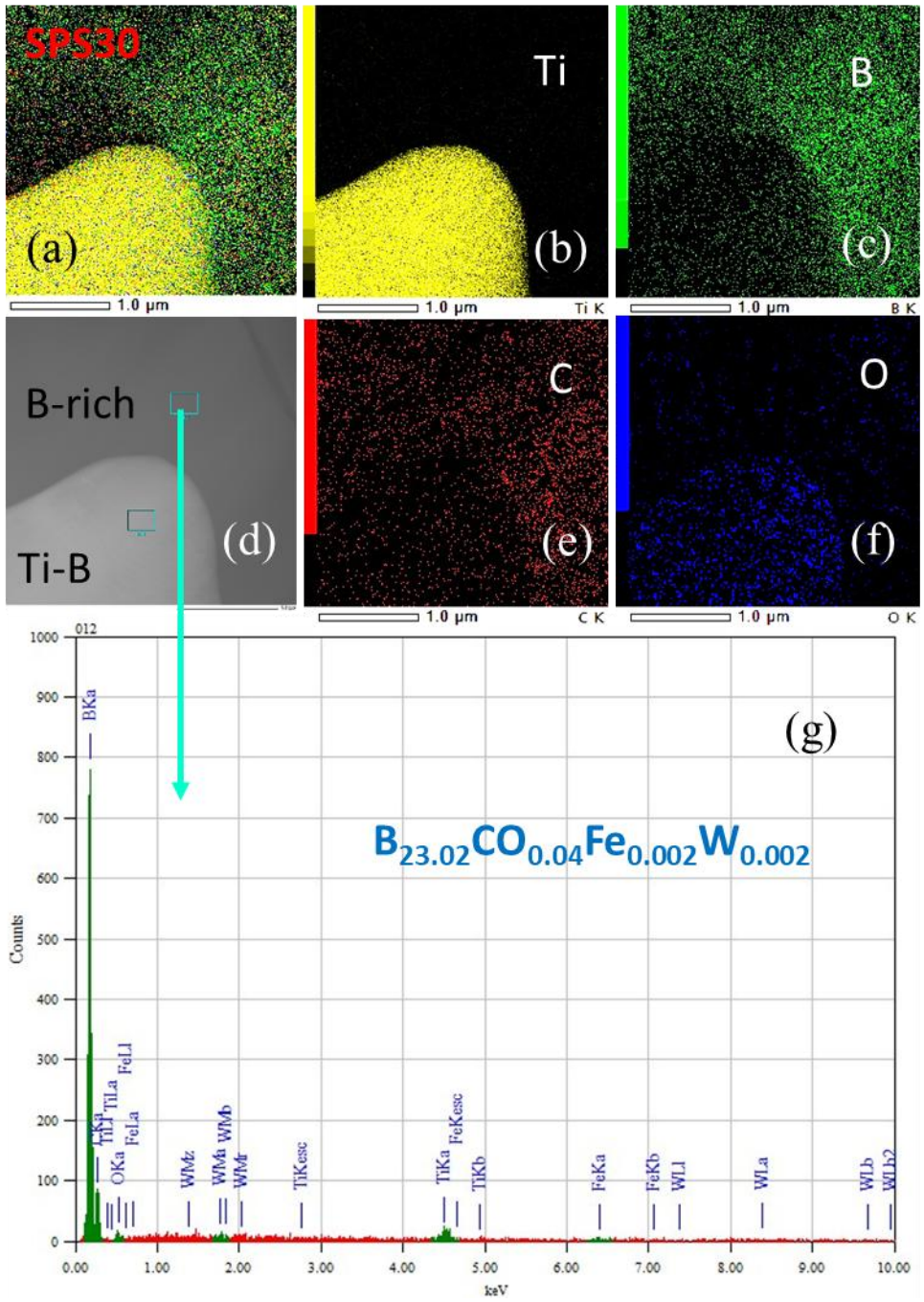

Fig. 1 Supplementary Material EDS elemental maps and spectrum in TEM on sample SPS30 showing a B-rich grain in proximity with a titanium boride grain.

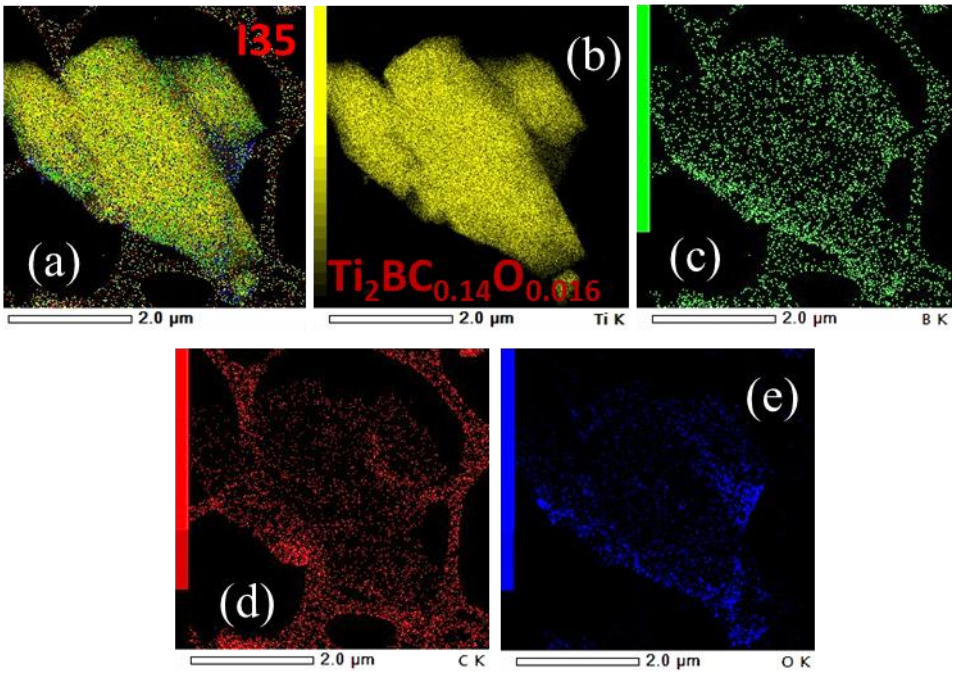

Fig. 2 Supplementary Material EDS maps in TEM showing a Ti-rich grain from sample I35.

***Declaration of Interest Statement**

Declaration of interests

☒ The authors declare that they have no known competing financial interests or personal relationships that could have appeared to influence the work reported in this paper.

☐The authors declare the following financial interests/personal relationships which may be considered as potential competing interests: